


Simulating Chemical Abundances in the Circumstellar Nebula of the Late Stage Binary RY Scuti

SARAH H. TAFT ¹, ROBERT D. GEHRZ,¹ CHARLES E. WOODWARD,¹ NATHAN SMITH,² ISABELLE PERRON,¹ AND ANNALISA CITRO¹

¹*Minnesota Institute for Astrophysics, University of Minnesota, 116 Church Street, Minneapolis, MN 55455, USA*

²*Steward Observatory, University of Arizona, 933 N. Cherry Avenue, Tucson, AZ 85721, USA*

ABSTRACT

RY Scuti, thought to be a Wolf-Rayet (WR) progenitor, is a massive, post-main-sequence, binary star system undergoing Roche lobe overflow (RLOF). SOFIA (+FORCAST) spectroscopy of the inner, ionized region of RY Scuti’s double ringed toroidal nebula affirms the previous detection of the well-studied 12.81 μm Ne II forbidden transition and reveals four distinct emission lines, including three previously undetected transitions, S III, Fe III, and S III. Cloudy photoionization modeling of the four neon, sulfur, and iron lines was performed to derive fractional abundances ($\log(\frac{X}{H})$) of neon at -3.19 ± 0.0251 , sulfur at -3.76 ± 0.0487 , and iron at -2.23 ± 0.0286 . All three species are overabundant with respect to fiducial solar chemical abundances, especially iron. Our analysis suggests that the outer envelope of the primary star in the RY Scuti system is being stripped away via RLOF, leaving helium-rich and hydrogen-poor material visible to observation. This material also exhibits elevated neon, sulfur, and iron fractional abundances, consistent with RY Scuti evolving toward a WR object.

1. INTRODUCTION

RY Scuti (HD 169515) is a massive, post-main-sequence, eclipsing binary system. The first detection of the forbidden Fe III transition (Edlen & Swings 1939) was in RY Scuti. Located at a distance of 1.8 ± 0.1 kpc (King & Jameson 1979; Smith et al. 2001, 2002), RY Scuti’s eclipsing light curve indicates that it is undergoing late-stage RLOF (Antokhina & Cherepashchuk 1988; Djurašević et al. 2001; Melikian et al. 2010). The primary/donor star, the star whose mass is being stripped during RLOF, is a supergiant with spectral classification O9.7 Ibpe var (Walborn 1982). The secondary/receiving/companion star, the star that is accreting mass from the donor star, is likely an O5 star (Smith et al. 2011). Mass calculations for each stellar component of the system vary, with earliest studies reporting a combined mass over $100M_{\odot}$ (Popper 1943), while recent studies typically cite a primary (donor) mass of $\simeq 7\text{-}10 M_{\odot}$ and secondary (companion) mass of $\simeq 25\text{-}30 M_{\odot}$ (Skulskii 1992; Sahade et al. 2002; Grundstrom et al. 2007). Prior to RY Scuti’s current RLOF epoch, the primary star was likely the more massive star in the binary, having lost a significant portion of its mass to gravitational transfer (Smith et al. 2011).

RY Scuti is also known to host a compact, double-ringed, expanding, toroidal circumstellar nebula. The nebula is spatially resolved in images across multiple wavelengths, including radio with the Very Large Array

(VLA) (Gehrz et al. 1995), infrared with Keck I (Gehrz et al. 2001) and Keck II (Smith et al. 2011), and optical H α and [Si III] with the Hubble Space Telescope (HST) (Smith et al. 1999, 2001, 2002). The inner ring of the toroidal nebula is $\simeq 2800$ au in diameter. H α and [Si III] HST images map out strong recombination lines from hot, ionized gas, and radio images map out free-free radiation from the same gas (Gehrz et al. 2001). The outer ring of the nebula is $\simeq 3800$ au in diameter, and thermal emission reveals that it is primarily comprised of warm dust, potentially with a polycyclic aromatic hydrocarbon (PAH) component (Gehrz et al. 1995; Smith et al. 2011). The outer ring was ejected in 1754 ± 36 yr, and the inner, ionized ring in 1881 ± 4 yr (Smith et al. 2001). This subsequent ejection of what we now see as the inner, ionized ring allowed dust to form in the outer shell as the inner shell shielded the outer shell from hot, ionizing photons. The distance to the inner ring’s boundary is likely consistent with the system’s Strömgren radius (Gehrz et al. 1995; Smith et al. 1999). It is in this ionized region of RY Scuti’s nebula where observed IR forbidden emission lines, such as the well-studied 12.81 μm Ne II line (Gehrz et al. 1995), originate.

RY Scuti is thought to be an immediate Wolf-Rayet binary progenitor system due to its significant mass loss and mass transfer (Antokhina & Cherepashchuk 1988; Giuricin & Mardirossian 1981; Smith et al. 2002). In the near future, RY Scuti could evolve to resemble the

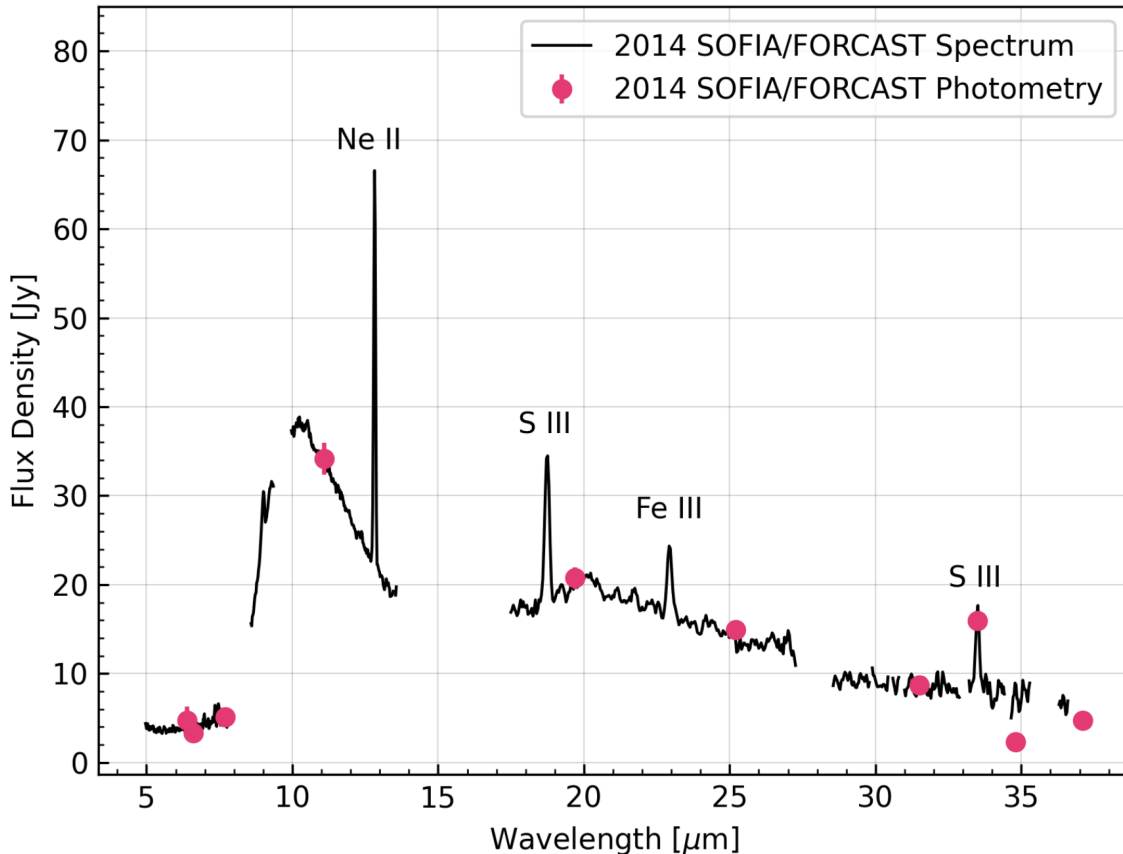


Figure 1. SOFIA multi-wavelength spectrum (solid black line) and photometry (filled pink circles). The spectrum is the data after telluric correction. Gaps in the spectrum across wavelength range are either due to wavelength regions not captured by the gratings or data filtered out during telluric correction. Line ionization states are labeled. The vertical pink lines overlaying the pink circles are the photometric error bars which, if not visible, are smaller than the plotting symbols. The continuum in both spectra is fueled by thermal emission from dust, and the significant feature at $10\mu\text{m}$ is likely due to silicate emission. There are no PAH emission lines at 7.7 or $11.3\mu\text{m}$.

very well studied γ^2 Vel system, with respective primary and secondary component masses of $9.0 \pm 0.6 M_{\odot}$ and $28.5 \pm 1.1 M_{\odot}$ (North et al. 2007). In these systems, stripping of the donor star’s outer envelope via RLOF will continue to reveal material in the star’s inner envelope and core that is extremely hydrogen depleted. Later in the star’s life, up to the days before it goes supernova, RLOF stripping will also reveal heavier metals such as sulfur and iron synthesized through oxygen and silicon burning (Grundstrom et al. 2007). The study of IR forbidden emission lines emitted by heavy metals in the ionized ring is therefore important. The $12.81\mu\text{m}$ Ne II line and other neon lines are especially important, as neon is the fourth most abundant element in WR stars, superseded only by oxygen, carbon, and helium (Smith & Houck 2005). Determination of metal abundances indicative of stellar evolutionary stage via concurrent study of photoionization simulation and spectral analysis yields insight into the evolutionary stage of RY Scuti, and extends to later stage stellar remnants as WR

systems themselves are progenitor systems of Type Ib/c supernovae (Tinyanont et al. 2019).

Here, we discuss a SOFIA (+FORCAST) study of RY Scuti. Section 2 describes the observations, both spectroscopic and photometric, Section 3 discusses the photoionization modelling (Cloudy; Chatzikos et al. 2023) of the RY Scuti IR spectrum and associated model parameters, Section 4 summarizes the model results and their significance, and Section 5 reiterates this study’s main conclusions.

2. OBSERVATIONS

2.1. Spectroscopy

A $5\text{--}37\mu\text{m}$ spectrum of RY Scuti was obtained on 2014 June 06 (program ID PID 02_0101; Arneson et al. 2018) using the NASA Stratospheric Observatory for Infrared Astronomy’s (SOFIA, Young et al. 2012) Faint Object infraRed Camera instrument for the SOFIA Telescope (FORCAST, Herter et al. 2018), a mid-infrared spectrograph and camera. Using the $4''7$ slit, all four FOR-

Table 1. SOFIA Integrated Line Intensities^{a)}

| Ion | Wavelength (μm) | Flux ($10^{-11} \text{ erg s}^{-1} \text{ cm}^{-2}$) | SNR | FWHM (μm) |
|--------|---------------------------------|---|------|---------------------------|
| Ne II | 12.83 | 6.653 ± 0.224 | 79.0 | 0.076 |
| S III | 18.74 | 2.831 ± 0.152 | 29.7 | 0.18 |
| Fe III | 22.94 | 1.001 ± 0.082 | 24.7 | 0.20 |
| S III | 33.50 | 0.381 ± 0.024 | 6.3 | 0.15 |

^{a)}The integrated IR line intensities derived from the SOFIA (+FORCAST) telluric-corrected spectrum (Figure 1) using Gaussian fits. The wavelength, FWHM, and SNR of each line is also included.

CAST gratings were employed, G063 (4.95 to 7.85 μm), G111 (8.59 to 13.72 μm), G227 (17.45 to 27.34 μm), and G329 (28.52 to 36.70 μm), with respective exposure times of 59.96s, 287.79s, 989.56s, and 1752.76s. Level 3 processed SOFIA data were retrieved from the IRSA archive¹, and are presented in Figure 1. Four forbidden transmission lines were detected, including three new lines (S III at 18.71 μm , Fe III at 22.92 μm , and S III at 33.47 μm) not identified in previous RY Scuti spectra (Gehrz et al. 1995).

In accordance with SOFIA grism line analysis techniques, a telluric correction beyond standard pipeline processing was applied to the data to mask any points with transmission ≤ 0.75 . The purpose of this additional masking was to exclude regions of the spectrum from model analysis that suffer from deep telluric absorption and thus a higher degree of uncertainty. This additional processing masked three other forbidden emission lines which are not presented in this work. While this reduced the total number of lines available for simulation and analysis, the remaining four lines have comparatively smaller uncertainties, leading to more reliable simulation results. The four remaining lines also represent all three elements observed in the original spectrum, so no element is excluded from this study due to telluric masking.

2.2. Integrated Line Intensities

Integrated line intensities found in the SOFIA spectrum were calculated by employing Python-based Astropy Gaussian fitters (Astropy Collaboration et al. 2013, 2018, 2022) to model the emission lines in the telluric corrected spectrum (Figure 1). Four individual Chebyshev polynomial continuum fit models were applied to and subtracted from each of the four wavelength regions observed by each of the four grisms. Inte-

grated line intensities were calculated by fitting a Gaussian function to each continuum subtracted emission line and integrating under the area of each respective curve. Errors were determined using the associated covariance matrices, with the square root of each diagonalized matrix corresponding to the uncertainty in each line. The signal-to-noise ratio (SNR) and full-width-half-maximum (FWHM) of each line were calculated using Specutils (Price-Whelan & et al. 2018). Integrated flux values, corresponding uncertainties, line SNR, and line FWHM are all reported in Table 1.

2.3. Photometry

Contemporaneous FORCAST imaging observations of RY Scuti were obtained as part of PID 02_0101. Images were obtained in ten narrow and board-band filters with effective wavelengths of 6.4, 6.6, 7.7, 11.1, 19.7, 25.2, 31.5, 33.5, 34.8, and 37.1 μm . Photometry of RY Scuti was performed in effective circular diameters chosen to be $\simeq 3$ times that of the cited FORCAST Cycle 7 point-spread function (PSF), with background aperture sizes $\simeq 2$ times larger. Errors were determined by adding the relative aperture flux error, relative flux calibration error, uncertainty in the flux calibration model at the observed wavelength, and the aperture error in the variance plane in quadrature, and multiplying by the background subtracted aperture flux. Eight individual images were taken at wavelength 6.4 μm , so the final photometric value was calculated by averaging, with errors added in quadrature. The final photometric values and uncertainties are depicted as filled pink circles in in Figure 1, with error bars represented by vertical lines. Individual photometric wavelengths, values, and uncertainties are reported in Table 2.

3. PHOTOIONIZATION MODEL

Given the presence of metallic forbidden lines in Figure 1, the spectral synthesis photoionization code Cloudy (Ferland et al. 2017; Chatzikos et al. 2023) was

¹ <https://irsa.ipac.caltech.edu/>

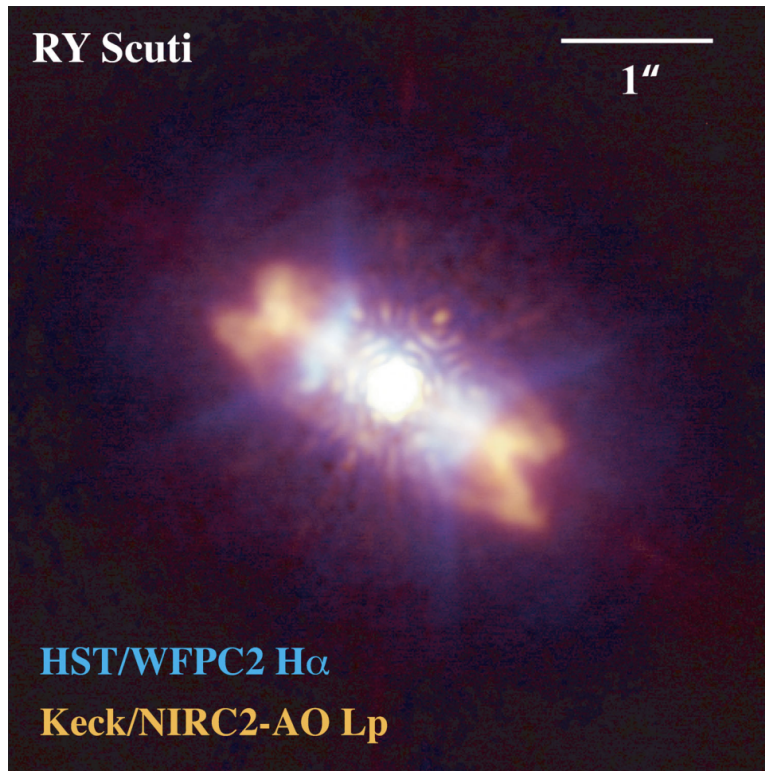


Figure 2. Reproduction of the color composite image of RY Scuti from [Smith et al. \(2011\)](#). The blue portion is $H\alpha$ emission, the region used to determine the best fit height and inner and outer radii values for the Cloudy nebular model. The orange portion is IR emission from dust. This image illustrates that dust and gas emission originate in separate regions of the nebula.

used for modeling. Cloudy works by solving statistical, thermal, and chemical equilibrium equations based on a variety of input parameters which quantify both the gas cloud responsible for line emission and the radiation source responsible for gas cloud excitation. Cloudy has been used to simulate photoionization in many different types of objects both similar and dissimilar to RY Scuti, from the mid-IR emission of planetary nebulae ([Gómez-Muñoz et al. 2024](#)), to metallicities of systems found in the circumgalactic medium ([Cristiani et al. 2024](#)), to modeling the ejecta in classical novae across multiple epochs of their post-outburst evolution ([Pandey et al. 2022](#); [Habtie et al. 2024](#)).

In this study, the radiation source is the dual blackbody emission by both stars in the RY Scuti binary, and the line-emitting gas cloud is the inner, ionized region of RY Scuti’s circumstellar nebula. Many model input parameters can be specified to characterize and quantify both the radiation source and emitting cloud, and those utilized in this study include effective blackbody temperature, blackbody luminosity, radially dependent cloud electron number density, cloud dust, cloud inner and outer radius, cloud height, cloud geometry, source distance, filling factor, covering factor, and cloud chemi-

cal abundances and depletion factors. For specific, quantified parameter values, see Section 3.1 and Table 3.

Initial models were created by exploring blackbody temperature, cloud electron number density, and filling factor values based off of canonical values and ranges found in the literature ([Lang 1992](#); [Gehrz et al. 1995](#); [Smith et al. 1999, 2002](#); [Men’shchikov & Miroshnichenko 2005](#); [Grundstrom et al. 2007](#); [Djurašević et al. 2008](#)). Exploration proceeded until the simulated integrated line intensities agreed with the observed integrated line intensities within an order of magnitude. Blackbody luminosity, cloud height, radius, geometry, covering factor, and source distance showed little variation in the literature and thus were chosen to remain static (i.e., without any initial experimentation). Models were assessed visually and those in clear disagreement with the observed SOFIA integrated line intensities were discarded and one or several parameter values were changed until agreement within an order of magnitude was reached.

Once order of magnitude agreement was reached between the synthetic spectrum and the observed spectrum, adjustments were made in the model helium abundance and hydrogen depletion to achieve order of magnitude agreement between the Cloudy model free-free continuum (green line in the right panel of Figure 3)

and the [Gehrz et al. \(1995\)](#) radio-extrapolated free-free continuum (black line in the left and right panels of Figure 3). The model free-free continuum was resistant to changes in all other system parameters; adjusting the helium abundance and hydrogen depletion proved to be the only successful method in aligning the model free-free continuum and the [Gehrz et al. \(1995\)](#) radio-extrapolated continuum.

Once order of magnitude agreement was reached between the synthetic spectrum, the observed spectrum, and the associated free-free continua, adjustments were made in the chemical abundances of the three elements (neon, sulfur, and iron) responsible for producing the four observed forbidden transition lines. Changes in neon, sulfur, and iron abundance had no discernible affect on the appearance of the model free-free continuum. Chemical abundances were initially set to solar levels as determined by [Lodders \(2021\)](#) and yielded models in poor agreement with the observed lines, as expected. Post-main sequence (PMS) values were also explored for non-free chemical abundances (i.e. elements other than helium, neon, sulfur, and iron) but showed no appreciable difference when compared with fiducial solar values and were therefore not used. Goodness of fit for each model spectrum was quantified by calculating a χ^2 value via the following relation:

$$\chi^2 = \sum_{i=1}^n \frac{(M_i - O_i)^2}{\sigma_i^2} \quad (1)$$

where M_i and O_i respectively represent the modeled and observed integrated line intensities, and σ_i represents the error in the observed integrated line intensities. The best model has the lowest χ^2 value, and was obtained via a minimization routine employing the Powell method. In this routine, the best fit model is obtained for all lines simultaneously, with each line weighted equally. A reduced chi square was also considered for this analysis but was ultimately rejected due to the model’s small number of degrees of freedom. Including each line’s FWHM in the χ^2 minimization was also considered, but was eventually rejected given the Cloudy’s model’s static (i.e. unchanging) resolution and therefore unchanging FWHM across varying chemical abundances. However, the observed and modeled FWHM values for each line are reported in Tables 1 and 4 respectively.

One- σ errors in the best fit chemical abundances were calculated by taking the standard deviation of the three ensembles of chemical abundance values iterated through during the χ^2 minimization process. Errors in the best fit integrated line intensities were calculated using a Monte Carlo simulation approach. One hundred models were simulated for each line, with chemical abun-

Table 2. Photometry Summary ^{b)}

| Wavelength (μm) | Flux (Jy) |
|---------------------------------|------------------|
| 6.4 | 4.74 ± 0.79 |
| 6.6 | 3.35 ± 0.11 |
| 7.7 | 5.12 ± 0.16 |
| 11.1 | 34.18 ± 0.89 |
| 19.7 | 20.74 ± 0.61 |
| 25.2 | 14.91 ± 0.47 |
| 31.5 | 8.72 ± 0.28 |
| 33.5 | 15.93 ± 0.47 |
| 34.8 | 2.34 ± 0.21 |
| 37.1 | 4.76 ± 0.23 |

^{b)} Summary of photometry values obtained alongside the newly reported RY Scuti spectrum in Figure 1.

dance values drawn from a random normal distribution with the mean set to the best fit chemical abundance value of each species and the standard deviation set to the associated 1σ error of each species. Chemical abundances were the only free parameters in the MC simulation. The standard deviation of each of these simulated ensembles is the error in the corresponding best fit integrated line intensity. The best fit chemical abundances, associated errors, and χ^2 value are reported in Table 3. The best fit model integrated line intensities, associated errors, adjacent free-free continuum, and line FWHM values are reported in Table 4 and can be seen in Figure 4.

3.1. Model Parameter Values

A temperature range between 25,000 K to 40,000 K was initially explored in increments of 1,000 K in Cloudy to determine first order-of-magnitude agreement between the synthetic and observed integrated line intensities. The most common temperature value cited for the primary star is 38,000 K ([Djurašević et al. 2008](#); [Grundstrom et al. 2007](#); [Lang 1992](#); [Smith et al. 1999](#)), and the most common temperature value cited for the secondary star is 30,000 K ([Djurašević et al. 2008](#); [Grundstrom et al. 2007](#); [Smith et al. 1999](#)). The aggregate temperature value employed in this work for the synthetically combined (i.e., singular simulated blackbody irradiating system) is 27,000 K, on the lower end of most values typ-

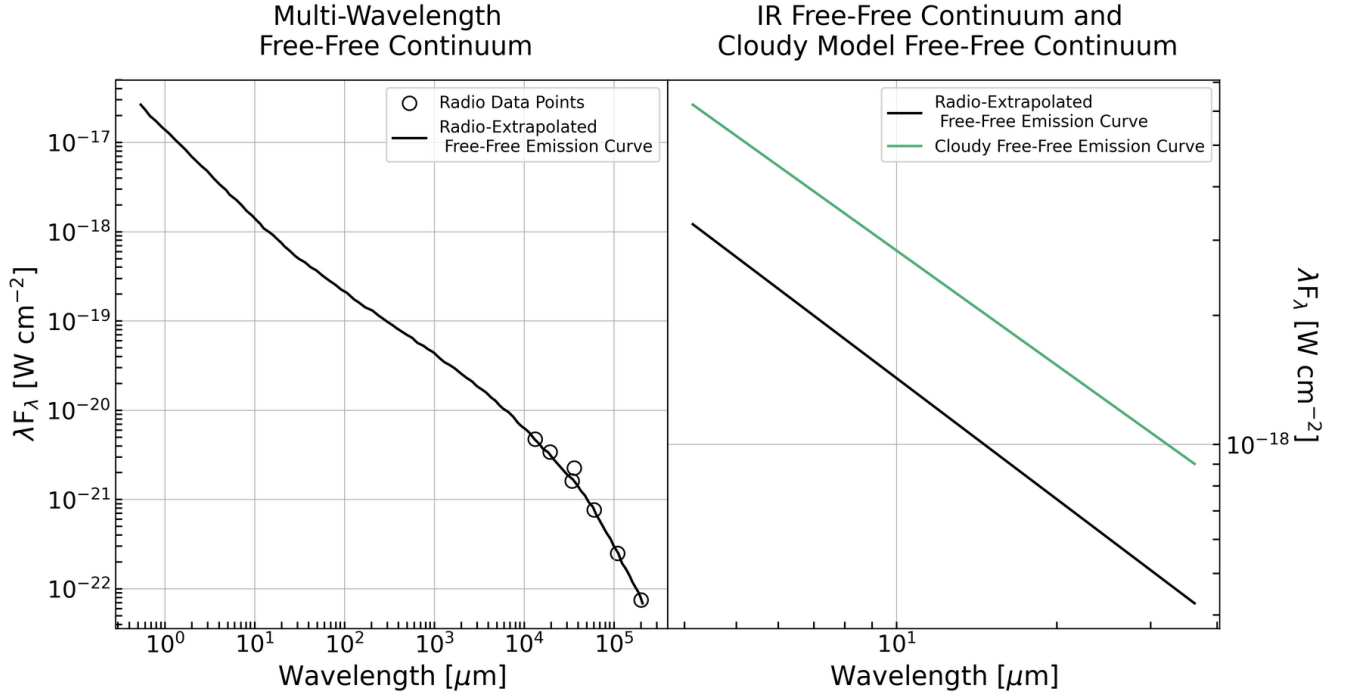


Figure 3. Left panel: Re-production of the radio data points and associated extrapolated thermal bremsstrahlung emission curve by a $T=8000$ K hydrogen nebula that becomes optically thick at 11cm from [Gehrz et al. \(1995\)](#). The deviation of the optically thin free-free slope from a λ^{-1} dependence at longer wavelengths is because the gaunt factor g becomes large ($\simeq 5.5$) at radio wavelengths. Right panel: The black line is the same free-free emission curve from the left panel shown only in the wavelength range explored in the Cloudy model. The green curve is the best fit power-law regression model of the free-free Cloudy continuum.

ically employed in the literature. However, this value is not unprecedented as [Men'shchikov & Miroshnichenko \(2005\)](#) use an identical value in their 2D-radiative transfer model of RY Scuti.

The bolometric luminosity of 1.36×10^{40} ergs is one of the static model parameters (i.e., not changed or treated as a free parameter), and is adopted following that cited in [Gehrz et al. \(1995\)](#).

Since the radius of the inner, ionized ring likely corresponds to the system's Strömgren radius, all of the modeled hydrogen gas is assumed to be ionized. Cloudy is capable of modeling the electron number density as either radially constant or radially dependent. In the case of radial dependency, the number density is defined as:

$$\frac{n(r)}{n(r_0)} = \left(\frac{r}{r_0}\right)^\alpha \text{ cm}^{-3} \quad (2)$$

where α denotes the exponent of the power law, $n(r)$ is the number density at a given radius, r , and $n(r_0)$ is the number density at the inner radius of the cloud, r_0 . Given that the toroidal nebula was created by a previous mass ejection event ([Grundstrom et al. 2007](#); [Smith et al. 2011](#)), and that the resulting mass in the

nebula is unlikely to be uniformly distributed as a result of this expulsion, radial dependence is assumed for the system's electron density. The corresponding power law exponent is chosen to be $\alpha = -3$ to ensure a steady mass per unit volume in the model shell (i.e., $\dot{M} = \text{constant}$).

The best fit value for the electron density at the ring's inner radius, r_0 , is $1 \times 10^6 \text{ cm}^{-3}$. While this is 5 times larger than the electron density of $2 \times 10^5 \text{ cm}^{-3}$ cited in [Smith et al. \(2002\)](#), the steep power law dependence allows the electron density to reach the [Smith et al. \(2002\)](#) value at a radius of $\simeq 790$ au, or $\simeq \frac{1}{3}$ of the way to the outer edge of the nebula.

Cylindrical geometry is assumed for the nebula, and inner radius, outer radius, and height, which define the boundaries of the cylindrical model, are adopted via visual inspection and trigonometric calculation from H α emission seen in the RY Scuti color composite image in [Figure 2](#). The inner shell radius is found to be 460 au and the outer radius is found to be 1385 au, similar to other values in the literature ([Gehrz et al. 1995](#); [Smith et al. 2001](#); [Grundstrom et al. 2007](#); [Smith et al. 2011](#)). The cloud's linear projected extent (i.e., height) is found to be 1360 au.

The expansion parallax (see [Mellema 2004](#)) of the ionized gas shell gives a distance of 1.8 ± 0.1 kpc, and the

Table 3. Best fitting Cloudy model parameters and accompanying χ^2 value.

| Parameters | Entry |
|--|--------------------|
| Blackbody temperature [K] | 27,000 |
| Luminosity [$\times 10^{40}$ ergs] | 1.36 |
| Initial electron number density [$\times 10^6$ cm $^{-3}$] | 1 |
| Inner radius [au] | 460 |
| Outer radius [au] | 1385 |
| Semi height [au] | 1360 |
| Distance [kpc] | 1.8 |
| Geometry | Cylindrical |
| Covering factor | 0.441 |
| Filling factor | 0.5 |
| Manually depleted hydrogen | 0.708 |
| Dust grains | None |
| Winds | None |
| Helium Abundance | -0.96 ± 0.0421 |
| Neon Abundance | -3.19 ± 0.0251 |
| Sulfur Abundance | -3.76 ± 0.0487 |
| Iron Abundance | -2.23 ± 0.0286 |
| χ^2 | 14.38 |

GAIA parallax gives a distance of 2.1 ± 0.1 kpc. A distance of 1.8 kpc is assumed since our calculations refer to observations of the expanding gas shell, in agreement with past literature values (King & Jameson 1979; Smith et al. 2001, 2002).

Given that RY Scuti is a PMS star exhibiting RLOF, and a likely WR progenitor, the system is hydrogen depleted. As such, the modeled hydrogen was manually depleted, and the best fit value is 0.708, or depletion by 29.2%.

A covering factor was found by determining the cylindrical model’s fractional projected surface area coverage on the sky. For simplicity, this area was calculated via:

$$\Omega = \frac{4\pi H}{\sqrt{H^2 + 4R^2}} \text{ sr} \quad (3)$$

where H is the cylinder’s height and R is the cylinder’s outer radius. This value was then divided by 4π steradians to determine the fractional coverage of 0.441, which is adopted as the covering factor value.

A canonical filling factor value of 0.5 is adopted to represent the not entirely smooth nor entirely clumpy distribution of gas in the inner, ionized nebula, as seen in Figure 2. While it’s possible this value accurately describes the degree of clumpiness in the system’s gas, degeneracy between filling factor and covering factor values could

also mean the filling factor is accidentally capturing the nebula’s ring structure. As illustrated by Smith et al. (1999), the ring structure in the gas precludes the nebula from covering the full extent of the cylinder’s projected surface area as suggested by the simplified model covering factor value of 0.441. This means the true filling factor could be higher than 0.5 (i.e., smoother gas), and the true covering factor could be lower than 0.441 (i.e., smaller fractional coverage).

Given that only the inner, ionized region of the nebula is modeled, and dust and gas emission originate in separate regions of the nebula as seen in Figure 2, no dust grains are included in the Cloudy model.

FORCAST gratings G063, G227, and G329 have a spectral resolution value of $R = 128$, with grating G111 at $R = 151$, resulting in resolvable velocities of $v = 2343$ km s $^{-1}$ for gratings G063, G227, and G329, and $v = 1986$ km s $^{-1}$ for grating G111. Expansion velocities of the inner, ionized ring are reported from 42 km s $^{-1}$ up to $\simeq 1000$ km s $^{-1}$ at the nebula’s poles (Smith et al. 2011), both notably smaller velocities than that which can be resolved in the spectrum. Stellar outflow (i.e., wind) is therefore not considered in the model.

4. RESULTS AND DISCUSSION

Figure 4 summarizes the results of the best fitting Cloudy model alongside the SOFIA observations. The black filled circles and associated error bars are the four observed SOFIA integrated line intensity values, summarized in Table 1, and the purple filled squares and associated errors are the χ^2 minimized (i.e., best fit) Cloudy model integrated line intensity values, summarized in Table 4.

The simulated Cloudy line intensity values for all ions agree with the observed SOFIA line intensities of the same species within errors. The simulated S III line at 33.4704 μm is most offset from its observed counterpart, and nearly in tension outside errors, with a percentage difference of 22%. In spite of this, the sulfur chemical abundance value that results in both sulfur line intensities remains the best fit abundance (i.e., χ^2 minimized).

Both sulfur lines at 18.7078 and 33.4704 μm are emission lines of the same ionization state, hence their intensities are both dependent on the same chemical abundance value. This linkage makes it impossible to increase one line flux value without increasing the other, or decrease one line flux value without decreasing the other. This posed a challenge given that the first simulated S III emission line was consistently larger than the observed emission line, and the second simulated S III emission line was consistently smaller than the observed emission line. Numerous attempts were made to improve

Table 4. Cloudy Integrated Line Intensities^{c)}

| Ion | Wavelength (μm) | Flux ($10^{-11} \text{ erg s}^{-1} \text{ cm}^{-2}$) | Adjacent Continuum ($10^{-11} \text{ erg s}^{-1} \text{ cm}^{-2}$) | FWHM (μm) |
|--------|---------------------------------|---|---|---------------------------|
| Ne II | 12.8101 | 6.682 ± 0.618 | 2.260 | 0.045 |
| S III | 18.7078 | 3.141 ± 0.289 | 1.621 | 0.065 |
| Fe III | 22.9190 | 0.957 ± 0.103 | 1.353 | 0.082 |
| S III | 33.4704 | 0.305 ± 0.028 | 0.971 | 0.12 |

^{c)}Best fit Cloudy model integrated line intensities with corresponding ion, wavelength, associated adjacent free-free continuum, and line FWHM values.

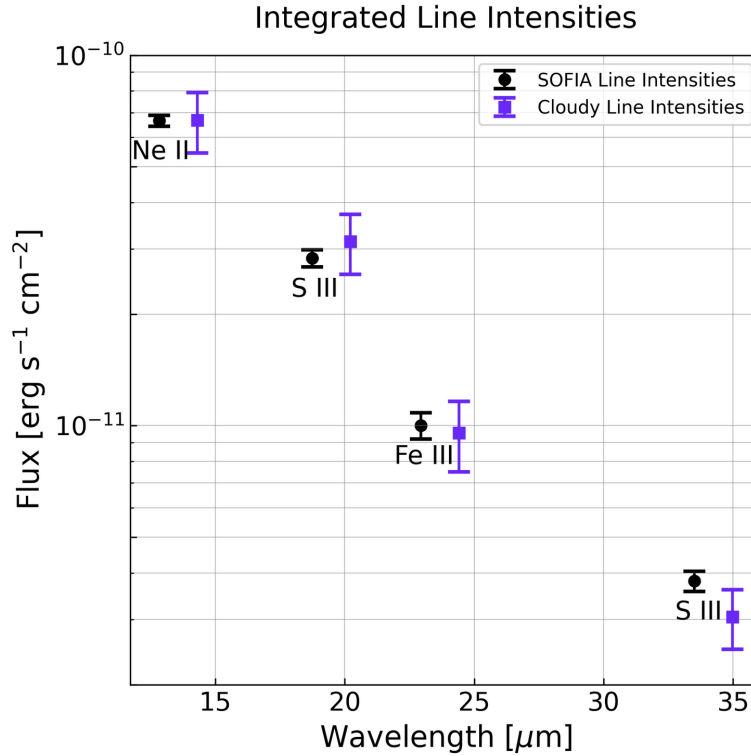


Figure 4. The black filled circles represent the SOFIA integrated line intensities and corresponding 1σ uncertainties. The purple filled circles are the best fit Cloudy model integrated line intensities and uncertainties calculated via Monte Carlo simulation. Wavelength offsets between the SOFIA and Cloudy lines are artificial and have been introduced solely for visual comparison and clarity, with the true wavelength for each ion corresponding to the black filled circle (i.e. the SOFIA line intensities). All model integrated line intensities are within SOFIA errors.

the model by increasing the sulfur abundance so the resulting intensities balanced the positive offset of the first line with the negative offset of the second more evenly than the reported best fit abundance. While these simulations provided the desired result, the accompanying χ^2 value was larger than the χ^2 value for the best fit chemical abundances. Those models were therefore rejected.

The primary result from this model is that all of the best fitting $\log \frac{N[x]}{N[H]}$ chemical abundance values are el-

evated above solar values, with neon at -3.19 ± 0.0251 compared to a solar value of -3.85 , sulfur at -3.76 ± 0.0487 compared to a solar value of -4.85 , iron at -2.23 ± 0.0286 compared to a solar value of -4.52 , and helium at -0.96 ± 0.0421 compared to a solar value of -1.076 (Lodders 2021). A summary of these values can be seen in Table 3.

Comparison of the Cloudy neon, sulfur, and iron abundances to fiducial Lodders (2021) solar abundances reveals that the three elements are respectively 4.57, 12.30,

and 194.98 times more abundant in the Cloudy model than in the solar model. Looking specifically at neon, Gehrz et al. (1995) propose an overabundance range with respect to solar fiducial values of 1.6-10. The 4.57 value falls within this range. Closer inspection reveals that Gehrz et al. (1995) reference a fiducial neon solar abundance of $\simeq -4.0$ as cited by Cameron (1982) and Anders & Grevesse (1989). The solar abundances listed in Lodders (2021) were used for this study, which cites a fiducial solar neon abundance of -3.85. By comparing the best fit neon value of -3.19 with the $\simeq -4.0$ value, neon proves overabundant by a factor of 6.45, still inside the Gehrz et al. (1995) proposed range but even higher.

Though at first glance, it may seem plausible to interpret the elevated neon, sulfur, and iron abundances as indicative of increased metallicity in the RY Scuti system, this is likely not the case. Neon is formed through helium capture by carbon and oxygen nuclei during the carbon-burning phase (Woosley et al. 2002). Sulfur and iron are produced later. Sulfur is created via the hydrostatic burning of neon which forms an oxygen convective core and produces elements up to ^{32}S (Lucertini et al. 2022). Iron is formed during the hydrostatic silicon-burning phase where silicon and other lighter elements undergo fusion in the core, ultimately forming elements up to ^{56}Fe (Golovaty & Skulskii 1992; Hix 1995). All three of these processes occur within the late stages of a star's evolution, with the carbon burning phase lasting a few hundred years, neon burning lasting about a year, and silicon burning lasting only about a day. Given that these abundances are observed in a nebula ejected approximately 100 years ago, and that RY Scuti has not yet gone supernova, it is unlikely that RY Scuti has created significant amounts of neon, let alone experienced oxygen or silicon burning.

Additionally, all abundances are listed relative to hydrogen ($\log(\frac{X}{H})$), meaning the hydrogen depletion factor also plays a role in explaining the overabundance of these three metals. The best fit helium abundance found to align the free-free continua is overabundant relative to fiducial solar levels by a factor of 1.31. Since helium is produced via hydrogen burning, the system is almost certainly hydrogen-depleted, a conclusion corroborated by the Cloudy model's 0.708 best fit hydrogen depletion value. While this depletion indeed contributes to boosting the observed elevated chemical abundances, the observed elevated abundances, especially of iron, cannot be explained by hydrogen depletion alone since the metals are elevated by factors that are both different from one another and larger than the factor by which hydrogen is depleted. Some enrichment factor other than in situ nu-

cleosynthesis must be at play. Thus, given its helium enhancement, hydrogen depletion, elevated metallic abundances, and continuous RLOF (Giuricin & Mardirossian 1981; Antokhina & Cherepashchuk 1988; Smith et al. 2002, 2011), RY Scuti remains a strong candidate for a WR progenitor system.

While these results affirm past postulations about RY Scuti's evolutionary stage, they are not infallible. The first avenue for improvement is exploring more robust mechanisms to constrain the hydrogen depletion and helium abundance. The bootstrapping from the radio free-free flux and comparing to IR emission lines is influenced by the relative helium abundance and hydrogen depletion factor, but may also be sensitive to other factors like ionization, temperature, or density inhomogeneities in the emission gas. Hence, over-interpretation of the derived helium abundance and hydrogen depletion is not warranted. One other possible avenue for improvement is the fact that the chemical abundances for neon and iron are determined based only on the integrated intensity of one spectral line, and sulfur based only on two. While the SOFIA spectrum used for this work precludes analysis of any other lines, making claims about chemical abundances in the system based only on one or two lines of the corresponding ionization state is not the most robust avenue for deriving conclusions. Future spectral analysis of RY Scuti should attempt to observe more forbidden transition lines of the elements in question. Other similar avenues for future work could include assessing emission lines from ionization states other than neon, sulfur, and iron, particularly those important to WR systems such as carbon and hydrogen; modeling RY Scuti using different photoionization software and cross checking with Cloudy; modeling the stars in RY Scuti as two individual blackbody sources as opposed to one singular source; and using a more robust fitting technique other than χ^2 minimization, such as log likelihood.

5. SUMMARY

By simulating archival SOFIA (+FORCAST) spectral lines of late-stage binary RY Scuti with photoionization software Cloudy, chemical abundances in the nebula's inner, ionized ring were determined. Respective values for the helium, neon, sulfur, and iron abundances are -0.96 ± 0.0421 , -3.19 ± 0.0251 , -3.76 ± 0.0487 , and -2.23 ± 0.0286 , with helium, neon, sulfur, and iron respectively 1.31, 4.57, 12.30, and 194.98 times more abundant than fiducial solar levels. This, in tandem with hydrogen depletion and ongoing RLOF, suggests that RY Scuti is a valid theorized WR progenitor system, caught at just the right time in its evolution to serve as an important

source of study for astrophysical knowledge of stellar evolution.

This research has made use of the NASA/IPAC Infrared Science Archive, which is funded by the National Aeronautics and Space Administration and operated by the California Institute of Technology. Based in part on observations made with the NASA/DLR Stratospheric Observatory for Infrared Astronomy (SOFIA). SOFIA is jointly operated by the Universities Space Research Association, Inc. (USRA), under NASA contract NNA17BF53C, and the Deutsches SOFIA Institut (DSI) under DLR contract 50 OK 2002 to the University of Stuttgart. RDG was supported, in part, by the United States Air Force. SHT would also like to thank Lindsey Gordon, John Hamilton Miller Jr., and Derek Perera for useful discussion and suggestions regarding this work.

Facilities: SOFIA (Young et al. 2012), FORCAST (Herter et al. 2018)

Software: Astropy (Astropy Collaboration et al. 2013, 2018, 2022), Cloudy (Chatzikos et al. 2023)

REFERENCES

- Anders, E., & Grevesse, N. 1989, *GeoCoA*, 53, 197
- Antokhina, E. A., & Cherepashchuk, A. M. 1988, *Soviet Astronomy Letters*, 14, 105
- Arneson, R. A., Shenoy, D., Smith, N., & Gehrz, R. D. 2018, *ApJ*, 864, 31
- Astropy Collaboration, Robitaille, T. P., Tollerud, E. J., et al. 2013, *A&A*, 558, A33
- Astropy Collaboration, Price-Whelan, A. M., Sipőcz, B. M., et al. 2018, *AJ*, 156, 123
- Astropy Collaboration, Price-Whelan, A. M., Lim, P. L., et al. 2022, *ApJ*, 935, 167
- Cameron, A. G. W. 1982, in *Essays in Nuclear Astrophysics*, ed. C. A. Barnes, D. D. Clayton, & D. N. Schramm, 23
- Chatzikos, M., Bianchi, S., Camilloni, F., et al. 2023, *RMxAA*, 59, 327
- Cristiani, S., Cupani, G., Trost, A., et al. 2024, *MNRAS*, 528, 6845
- Djurašević, G., Vince, I., & Atanacković, O. 2008, *AJ*, 136, 767
- Djurašević, G., Zakirov, M., Eshankulova, M., & Erkapic, S. 2001, *A&A*, 374, 638
- Edden, B., & Swings, P. 1939, *The Observatory*, 62, 234
- Ferland, G. J., Chatzikos, M., Guzmán, F., et al. 2017, *RMxAA*, 53, 385
- Gehrz, R. D., Smith, N., Jones, B., Puetter, R., & Yahil, A. 2001, *ApJ*, 559, 395
- Gehrz, R. D., Hayward, T. L., Houck, J. R., et al. 1995, *ApJ*, 439, 417
- Giuricin, G., & Mardirossian, F. 1981, *A&A*, 101, 138
- Golovatyi, V. V., & Skulskii, M. Y. 1992, *Soviet Ast.*, 36, 550
- Gómez-Muñoz, M. A., García-Hernández, D. A., Barzaga, R., Machado, A., & Huertas-Roldán, T. 2024, *A&A*, 682, L18
- Grundstrom, E. D., Gies, D. R., Hillwig, T. C., et al. 2007, *ApJ*, 667, 505
- Habtie, G. R., Das, R., Pandey, R., Ashok, N. M., & Dubovsky, P. A. 2024, *MNRAS*, 527, 1405
- Herter, T. L., Adams, J. D., Gull, G. E., et al. 2018, *Journal of Astronomical Instrumentation*, 7, 1840005
- Hix, W. R. 1995, PhD thesis, Harvard University, Massachusetts
- King, A. R., & Jameson, R. F. 1979, *A&A*, 71, 326
- Lang, K. R. 1992, *Astrophysical Data I. Planets and Stars*.
- Lodders, K. 2021, *SSRv*, 217, 44
- Lucertini, F., Monaco, L., Caffau, E., Bonifacio, P., & Mucciarelli, A. 2022, *A&A*, 657, A29
- Melikian, N. D., Tamazian, V. S., Docobo, J. A., et al. 2010, *Astrophysics*, 53, 202
- Mellema, G. 2004, *A&A*, 416, 623
- Men'shchikov, A. B., & Miroshnichenko, A. S. 2005, *A&A*, 443, 211

- North, J. R., Tuthill, P. G., Tango, W. J., & Davis, J. 2007, *MNRAS*, 377, 415
- Pandey, R., Das, R., Shaw, G., & Mondal, S. 2022, *ApJ*, 925, 187
- Popper, D. M. 1943, *ApJ*, 97, 394
- Price-Whelan, A. M., & et al. 2018, *Specutils: A Python Package for Spectroscopic Analysis*, Zenodo
- Sahade, J., West, R. M., & Skul'Sky, M. Y. 2002, *RMxAA*, 38, 259
- Skulskii, M. Y. 1992, *Soviet Ast.*, 36, 411
- Smith, J.-D. T., & Houck, J. R. 2005, *ApJ*, 622, 1044
- Smith, N., Gehrz, R. D., Campbell, R., et al. 2011, *MNRAS*, 418, 1959
- Smith, N., Gehrz, R. D., & Goss, W. M. 2001, *AJ*, 122, 2700
- Smith, N., Gehrz, R. D., Humphreys, R. M., et al. 1999, *AJ*, 118, 960
- Smith, N., Gehrz, R. D., Stahl, O., Balick, B., & Kaufer, A. 2002, *ApJ*, 578, 464
- Tinyanont, S., Lau, R. M., Kasliwal, M. M., et al. 2019, *ApJ*, 887, 75
- Walborn, N. R. 1982, *AJ*, 87, 1300
- Woosley, S. E., Heger, A., & Weaver, T. A. 2002, *Reviews of Modern Physics*, 74, 1015
- Young, E. T., Becklin, E. E., Marcum, P. M., et al. 2012, *ApJL*, 749, L17